

Effects of the Low Reynolds Number on the Loss Characteristics in a Transonic Axial Compressor

Minsuk Choi¹, Seong Hwan Oh², Han Young Ko² and Je Hyun Baek¹

¹Graduate student and professor in POSTECH, San 31, Hyoja-dong, Pohang, 790-784, South Korea
choims@postech.ac.kr / jhbaek@postech.ac.kr

²Researchers, Agency for Defense Development, Yuseong P.O.B(No.) 35, Daejeon, 305-600, South Korea
osh0705@add.re.kr / hanyko@add.re.kr

Keywords: Low Reynolds Number, Loss, Shock, Transonic Axial Compressor

Abstract

A three-dimensional computation was conducted to understand effects of the low Reynolds number on the loss characteristics in a transonic axial compressor, Rotor67. As a gas turbine becomes smaller in size and it is operated at high altitude, the operating condition frequently lies at low Reynolds number. It is generally known that wall boundary layers are thickened and a large separation occurs on the blade surface in axial turbomachinery as the Reynolds number decreases. In this study, it was found that the large viscosity did not affect on the bow shock at the leading edge but significantly did on the location and the intensity of the passage shock. The passage shock moved upstream towards leading edge and its intensity decreased at the low Reynolds number. This change had large effects on the performance as well as the internal flows such as the pressure distribution on the blade surface, tip leakage flow and separation. The total pressure rise and the adiabatic efficiency decreased about 3% individually at the same normalized mass flow rate at the low Reynolds number. In order to analyze this performance drop caused by the low Reynolds number, the total pressure loss was scrutinized through major loss categories such as profile loss, tip leakage loss, endwall loss and shock loss.

1. Introduction

The Reynolds number based on the operating condition of the gas turbine has become smaller recently, because the size of the gas turbine and its component has diminished and the needs to operate the existing gas turbine at high altitude have increased. As the Reynolds number is reduced, the wall boundary layers are thickened and the large separation occurs on the blade surface. Since these deteriorations of the internal flow have bad effects on the performance in an axial turbomachinery, much attention has been paid to investigate the effects of the low Reynolds number on the axial turbomachinery.

In the design sense, the low Reynolds number condition is frequently attributed to the low air density at high altitude. Weinberg and Wyzykowski⁽¹⁾ at Pratt & Whitney Canada have conducted experimental studies on the effects of the low Reynolds number on

the gas turbine engine in cooperation with NASA. The PW545 jet engine, originally designed to operate at the 13.7km altitude, was tested above 18.3km in the air. They have reported that the efficiency and performance of the engine are diminished by the low air density at high altitude. Castner et al.⁽²⁾ have compared their numerical studies to the experimental data of Weinberg and Wyzykowski⁽¹⁾ in regard to the low Reynolds number. The calculated efficiency and performance showed good agreements with test data within the range of the Reynolds number from 30,000 to 295,000. Schreiber et al.⁽³⁾ did a research about the transition phenomena on the blade surface in a compressor cascade, changing the Reynolds number and the turbulence intensity. They have reported that a laminar separation bubble with reattachment is visible on the suction surface at a relatively low Reynolds number. After a wind tunnel test within the range of the Reynolds number from 25,000 to 50,000, Van Treuren et al.⁽⁴⁾ have reported that a large separation near the trailing edge of the turbine cascade has a bad effect on the total pressure loss. Matsunuma⁽⁵⁾ has conducted a wind tunnel test for the turbine cascade with the tip clearance, and analyzed the relation between the tip leakage flow, the Reynolds number and the turbulence intensity. He has shown that the Reynolds number and free-stream turbulence intensity have no effect on the tip clearance loss of the turbine cascade although they change the distributions of the internal flow. Matsunuma and Tsutsui⁽⁶⁾ have conducted an experiment about the change of the total pressure loss of a small one-stage axial turbine caused by the low Reynolds number from 32,000 to 128,000. They have reported that the region of high turbulence intensity due to the wake and the flow fluctuation due to the stator-rotor interaction increase with the decreasing Reynolds number.

Although there are a few studies on the effect of the low Reynolds number on the internal flow in the turbomachinery, most of them have focused on the flow phenomena but not on the loss characteristics. After an extensive numerical simulation, Choi et al.⁽⁷⁾ have analyzed the effects of the Reynolds number on the profile loss, tip leakage loss and end-wall loss in a subsonic axial compressor and reported that the tip leakage loss reduces for lower Reynolds number due to weaker mixing of the tip leakage and mainstream flows. However, in a transonic compressor, the

internal flow is more complicated due to the interaction between the tip leakage flow and the rotor passage shock, according to the previous results of several authors (Adamczk et al.⁽⁸⁾, Copenhaver et al.⁽⁹⁾, Masaki and Kaji⁽¹⁰⁾, Chima⁽¹¹⁾, Gerolymos and Vallet⁽¹²⁾, Hoeger et al.⁽¹³⁾, Park et al.⁽¹⁴⁾). So, the loss characteristics in a transonic compressor is a little bit different from that in a subsonic compressor. The present study investigates the effects of the low Reynolds number on the loss characteristics in a transonic compressor through numerical simulations. By applying Denton's loss model⁽¹⁵⁾ to the computational results, a comprehensive analysis of the loss mechanism is attempted.

2. Test Configuration

2.1 Compressor rotor

We conducted a numerical study of the effect of the low Reynolds number on the internal flow and the loss characteristics using a transonic axial compressor, Rotor67, which was tested by Strasizer et al.⁽¹⁶⁾ at NASA Lewis. Figure 1 shows the schematic diagram of the Rotor67 and the measurement locations. This rotor rotates about its axis at 16,043rpm with a tip Mach number of 1.38. The mass flow rates and pressure ratios between the inlet and outlet are 33.25kg/s and 1.63 at the design condition respectively. The Reynolds number is about 1.17×10^6 , which was based on the inlet velocity at the design condition and the meridional line on the hub. This rotor has 22 blades and an aspect ratio of 1.56. Detailed design parameters are summarized in Table 1. Radial distribution of static and total pressure, total temperature and the flow angle along the span were measured at aero-stations 1 and 2 located upstream and downstream of the rotor.

2.2 Computational grid

By using the blade profile given by Strasizer et al.⁽¹⁶⁾, a computational domain was fixed in the region

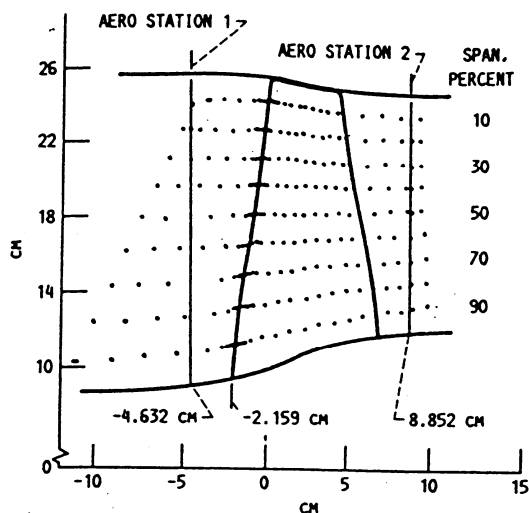


Fig. 1 Schematic diagram of Rotor67 showing measurement positions

Table 1 Design parameter of Rotor67

Number of rotor blades		22
Rotational speed (rpm)		16,043
Mass flow (kg/s)		33.25
Pressure ratio		1.63
Rotor tip speed (m/s)		429
Tip clearance at design speed (cm)		0.061
Inlet tip relative mach number		1.38
Rotor aspect ratio		1.56
Rotor solidity	Hub	3.11
	Tip	1.29
Tip diameter (cm)	Inlet	51.4
	Exit	48.5
Hub/Tip radius ratio	Inlet	0.365
	Exit	0.478

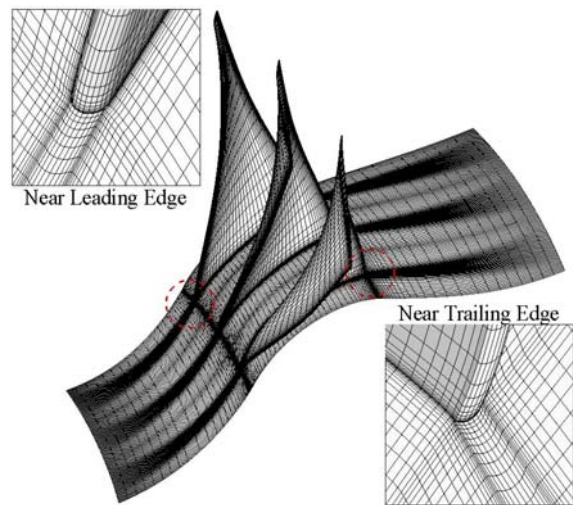


Fig. 2 Computational grid for Rotor67

including aero-stations 1 and 2, and a multi-block hexahedral mesh was generated as shown in Fig. 2. Each passage consists of 117 nodes in the streamwise direction, 57 nodes in the pitchwise direction, and 53 nodes in the spanwise direction. To capture the tip leakage flow correctly, the region of the tip clearance was filled with the embedded H-type grid, which has 52 nodes from the leading edge to the trailing edge, 9 nodes across the blade thickness and 9 nodes from the blade tip to the casing. Therefore, the computational domain has a total of about 350,000 nodes.

2.3 Numerical method

Simulations of the three-dimensional flow were conducted using the in-house flow solver, TFlow. The TFlow has been improved to calculate the internal flow in turbomachinery since its development in the mid-1990s⁽¹⁷⁾. This flow solver has been validated through a series of calculations of the transonic axial compressor, the subsonic axial compressor and the subsonic axial turbine until now.^(14, 18-19) The TFlow uses the compressible RANS (Reynolds Averaged Navier-Stokes) equations. The governing equations were discretized in space by the finite volume method. An upwind TVD (Total Variational Diminishing) scheme based on Roe's flux difference splitting method was used to discretize the inviscid flux terms and the MUSCL (Monotone Upstream Centered

Scheme for Conservation Law) technique was used for interpolation of flow variables. The second order central difference method was used to discretize the viscous flux terms. The equation was solved using the Euler implicit time marching scheme with first order accuracy to obtain a steady solution. The laminar viscosity was calculated by Sutherland's law and the turbulent viscosity was obtained by the algebraic Baldwin-Lomax model⁽²⁰⁾ because the flow field was assumed to be fully turbulent.

2.4 Boundary conditions and Reynolds number

In the internal flows simulation of turbomachinery, there are four different types of boundaries such as inlet, outlet, wall, and periodic conditions. The total pressure, total temperature, whirl, and meridional flow angle were fixed at the inlet condition and the upstream-running Riemann invariant was extrapolated from the interior domain. The inlet total pressure was specified as a constant in the core flow and reduced in the endwall regions according to a 1/7 power law velocity profile. The inlet boundary layer thickness on the hub and the casing was set to be 12mm, which was estimated from the experimental data. The inlet total temperature was specified as a constant. The whirl velocity, v_θ , was set to be zero, and the radial velocity, v_r , was chosen to make the flow to be tangent to the meridional projection of the inlet grid lines. For the outlet condition, the static pressure on the hub was specified and the local static pressures along the span were given by using the SRE (Simplified Radial Equilibrium) equation like Eq. (1). Other flow variables such as density and velocities were extrapolated from the interior.

$$\frac{\partial p}{\partial r} = \frac{\rho v_\theta^2}{r} \quad (1)$$

In order to calculate the velocity components on the wall, the relative velocities were set to be zero on the blade surface and the rotating part of the hub and the absolute velocities on the casing and the stationary part of the hub as the no-slip condition. The surface pressure and the density were obtained using the normal momentum equation and the adiabatic wall condition respectively. Since only one blade passage was used in the steady simulation, the periodic condition was implemented using the ghost cell next to the boundary cell and it enabled flow variables to be continuous across the boundary.

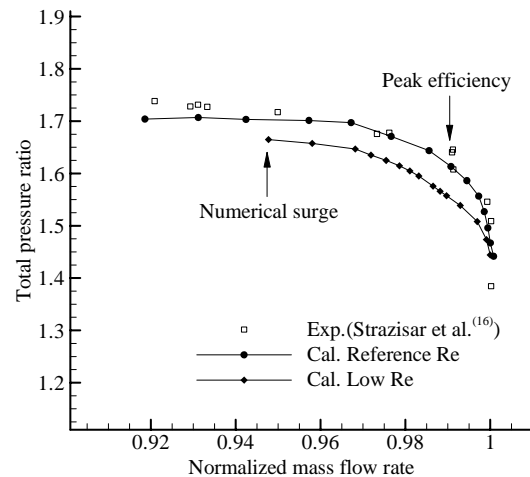
Referring to the U. S. standard atmosphere⁽²¹⁾, the density and viscosity at the 20km altitude are reduced in the ratio 1 to 0.07 and 1 to 0.77 respectively in comparison to the values at the sea level. The Reynolds number at the 20km altitude becomes a tenth of that at the sea level, if other operating conditions except for the density and viscosity are identical. Therefore, simulations were conducted at two Reynolds number, 1.17×10^5 and 1.17×10^6 , changing the back pressure but keeping other conditions same. We assigned the former to "Low

Reynolds number" or "Low Re", and the latter to "Reference Reynolds number" or "Ref. Re" for notational convenience.

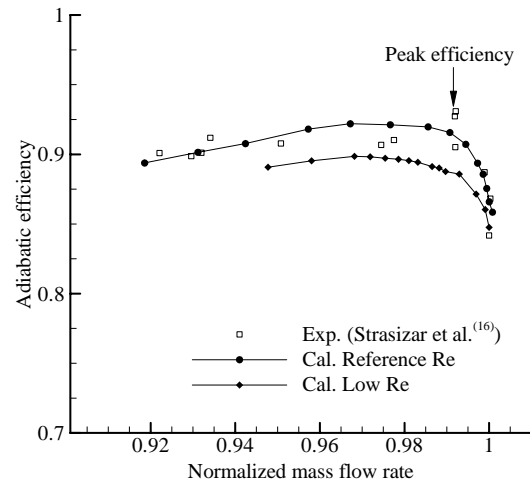
3. Computational Result

3.1 Internal flows

To find the change of the performance of Rotor67 caused by low Reynolds number, performance curves computed at design speed are shown in Fig. 3, where the horizontal axis was represented by the normalized mass flow rate. The normalized mass flow rate is defined by the ratio of the mass flow rate to the mass flow rate at choke and it could remove some uncertainties of measuring the mass flow rate in the experiment. The choking mass flow rate was 34.96kg/s in the experiment and the 34.57kg/s in the simulation of the reference Reynolds number, where the discrepancy between these values was within 1 percent. The total pressure ratio obtained by the numerical simulation corresponds to the experimental one at the reference Reynolds number very well. The total pressure ratio at low Reynolds number has a decrease of about 3 percent at the same normalized mass flow rate, compared with the reference Reynolds number. This means that some additional losses



(a) Total pressure ratio curve



(b) Adiabatic efficiency curve

Fig. 3 Performance curves of Rotor67

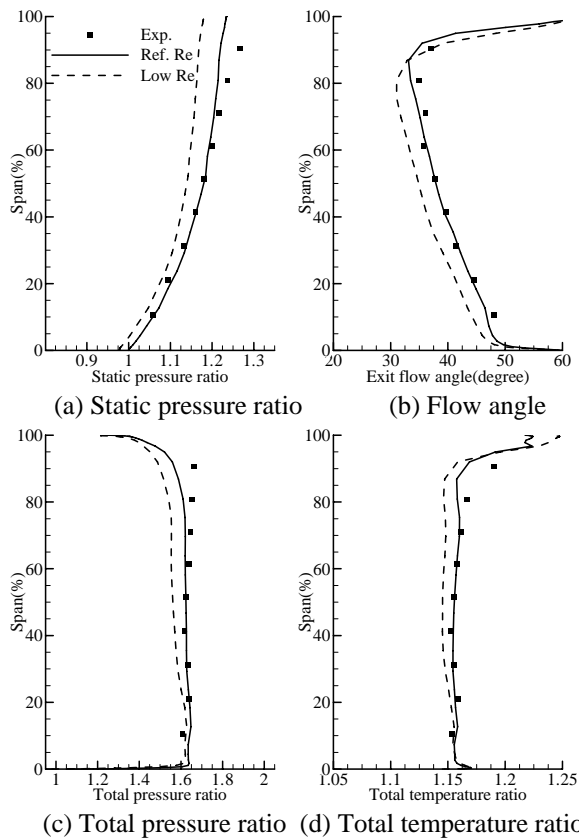


Fig. 4 Exit flow data along the span at aero-station 2 for peak efficiency

are generated in the internal flows or the rotor does not work on the fluid properly due to the large viscosity. The numerical surge occurs at high normalized mass flow rate and this makes the operating range of Rotor67 to be severely decreased. The adiabatic efficiency agrees well between the computation and experiment, even though the peak efficiency point slightly deviates from the experimental one. There is also about 3 percent drop of the adiabatic efficiency as the Reynolds number is reduced. This decrement of the efficiency is nearly same as that of the total pressure ratio.

Figure 4 shows the spanwise distributions of the mass-averaged static pressure and total pressure, total temperature and exit flow angle with experimental data at the peak efficiency condition. The pressure and the temperature are represented by the ratio to the inlet total pressure and the inlet total temperature respectively. The computed values for the reference Reynolds number have a good agreement to the experimental one although the static and total pressure values are slightly under-predicted near the casing. At the reference Reynolds number, the static pressure becomes large along the span from the hub to the casing due to the centrifugal force. The flow angle decreases along the span from the hub to the 90% span from the hub, but it is abruptly under-turning due to the blockage of the tip leakage flow near the casing. The total pressure and temperature are nearly constant in the core flow region, but the former is decreased and the latter is increased near the casing due to the tip

leakage flow. This means that tip leakage flow generates large loss in this region. At the low Reynolds number, static pressure is decreased in comparison to that of the reference Reynolds number. The discrepancy is small from the hub to the 50% span but a little bit large above 50% span. The flow angle is over-turning from the hub to the 90% span but under-turning near the casing. The total pressure becomes small as the Reynolds number decreases and this means Rotor67 couldn't properly transfer mechanical energy to the aerodynamic energy. The total temperature is nearly constant along the full span and a little bit small relative to the value of the reference Reynolds number.

Figure 5 shows the comparisons of the experimental and computed relative Mach number contours at 30%, 70% and 90% spans from the hub for the peak efficiency. The calculated values at the reference Reynolds number agree well with the experimental values and a shock structure is clearly observed. The shock system has a lambda structure with a bow shock at the front region of the blades. The passage shock, which crosses the blade channel, is generated above 70% span. This passage shock implies the flow is locally choked at each span, while Rotor67 is not fully choked yet. The boundary layers on the blade surface grow rapidly at the downstream of the passage shock, because the velocity magnitude abruptly decreases and the static pressure increase after the flow is across the shock. The flow at 30% span from the hub is well-behaved without the passage shock even though the flow field has a small supersonic region at the leading edge. At the low Reynolds number, the relatively large viscosity adds a dissipative effect to the flow field but it does not significantly affect the bow shock at the leading edge because the flow field upstream of the bow shock is nearly inviscid flow. On the contrary, the passage shock has some changes due to the relatively large viscosity. Firstly, the passage shock at 70% and 90% spans from the hub moves upstream to the leading edge. Therefore, the boundary layer develops at the more upstream point than that of the reference Reynolds number and separations occur in the boundary layer on the suction surface at the trailing edge. Second, the mach number contours show that the flow is still locally choked at these spans but the intensity of the passage shock becomes weak referring to the wide-spread contour lines. The pressure jump across this weak shock becomes small and it makes the static pressure in this region to have small value. The overall flow field at 30% span from the hub has a similar feature regardless of Reynolds number, but the flow between blades is more diffused by the large viscosity.

Figure 6 shows the static pressure distribution on the blade surface at several spanwise positions for the peak efficiency, where it was non-dimensionalized by the inlet total pressure. This distribution clearly shows the position of the passage shock and the load variation in streamwise direction at each span. While there is no shock from the hub to the 50% span, above

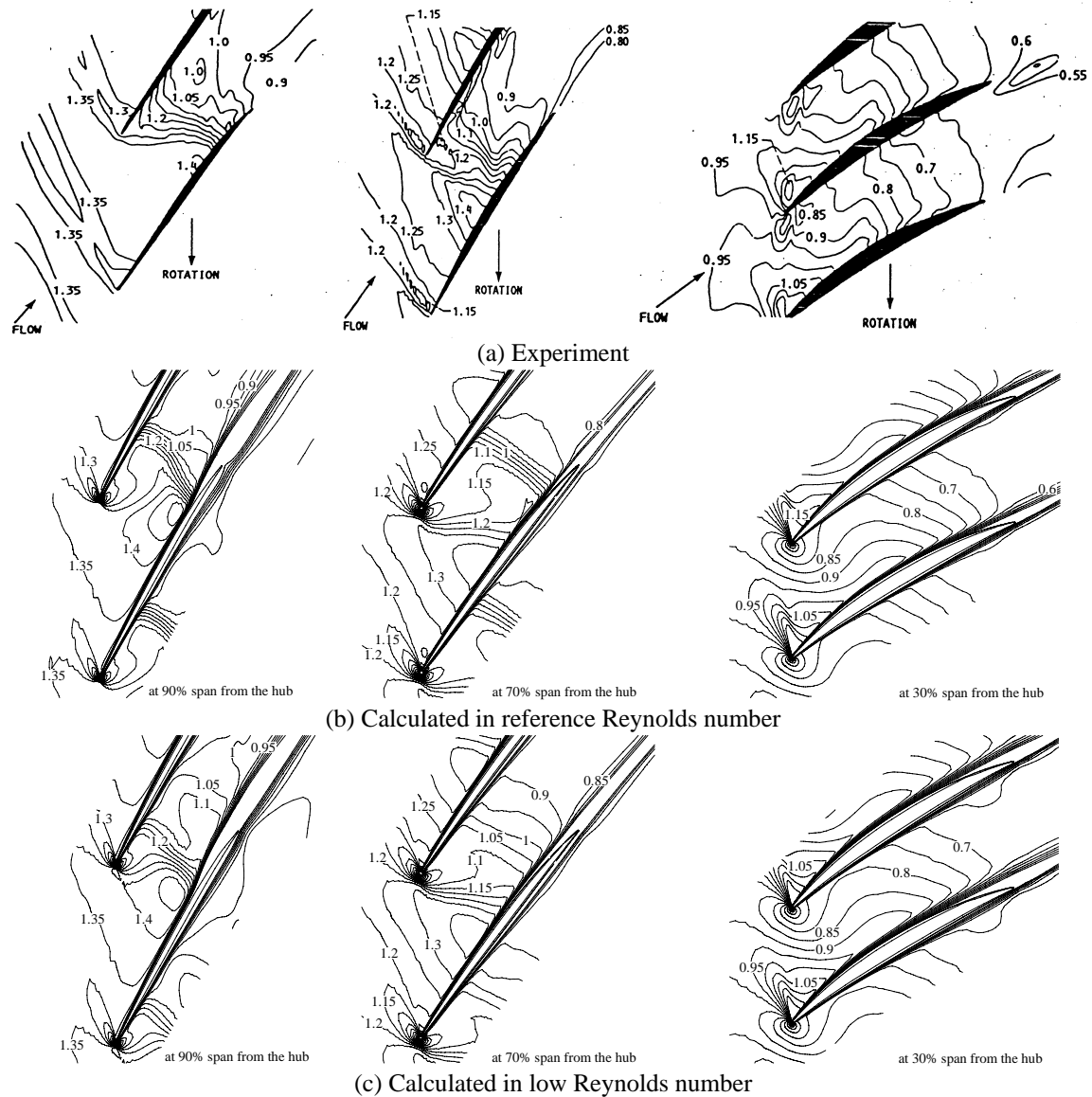


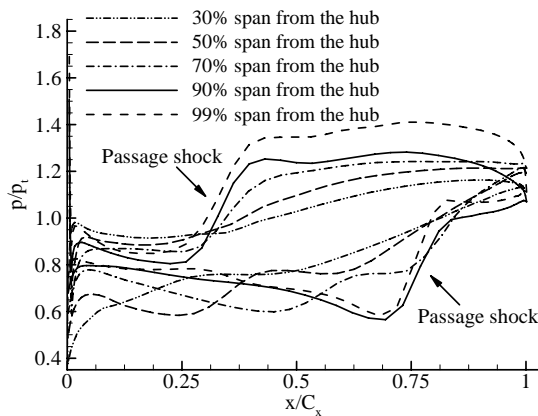
Fig. 5 Relative Mach number contours for peak efficiency

70% span from the hub, the pressure jump occurs at 30% chord from the leading edge on the pressure side leg and at 80% chord on the suction side leg of the passage shock. The static pressure distribution on the blade surface near the casing is very important because the pressure difference across the blade is the driving force for the tip leakage flow. At the 99% span from the hub, the static pressure on the pressure surface rapidly grows large due to the passage shock and it is nearly constant behind the pressure side leg of the shock. The static pressure on the suction surface is continuously decreasing and it increases behind the suction side leg of the shock. The pressure difference abruptly increases just behind the pressure side leg and has the maximum value just before the suction side leg of the passage shock. Therefore, the strong roll-up of the tip leakage flow is generated at the 30% chord at the reference Reynolds number. At the low Reynolds number, each leg of the passage shock on blade surfaces moves upstream, so the pressure side leg is at the 20% chord and the suction side leg at the 70% chord from the leading edge.

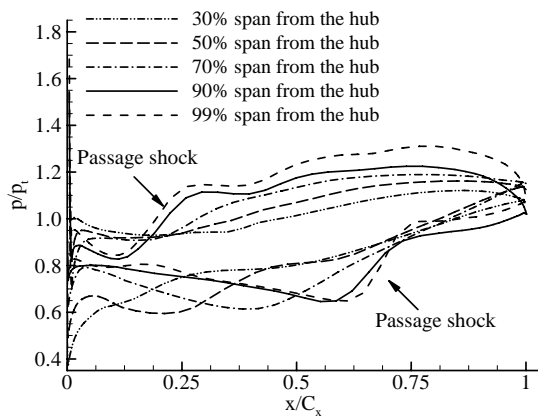
The pressure jump is small because the passage shock is weaker than that at the reference Reynolds number. At the 70% span from the hub, the effect of the passage shock so small that it is not easy to detect the passage shock in the pressure distribution. Near the casing, the pressure difference has large values between the pressure and the suction side legs of the passage shock even though the value is smaller than that at the reference Reynolds number. This small difference makes the tip leakage flow to be weak and the formation of the vortex center to be retarded.

The tip leakage flow is generated by the pressure difference between the pressure and suction surfaces near the casing. Figure 7 shows the distribution of the static pressure near the casing, center of the tip leakage flow (A) and particle traces ejected around the tip leakage flow center (B), where the traces are colored by the normalized helicity. The normalized helicity has a value near 1 or -1 at the center of the tip leakage flow. In two cases displayed in Fig. 7, the trajectory of the center coincides with the static

pressure trough and it has values of the normalized helicity near -1. The pressure trough becomes deep as the Reynolds number increases and this means that the tip leakage flow is stronger at the reference Reynolds number. The center of the tip leakage flow in both cases starts near the pressure side leg of the passage shock where the pressure difference across the blade increase rapidly, because this point is located behind the shock on the pressure surface but still before the shock on the suction surface. Therefore, the starting point of the tip leakage flow at the reference Reynolds number is located behind that at low Reynolds number. At the reference Reynolds number, the particle traces are concentrated on the vortex center at the start but they abruptly have spiral motion after passing the passage shock. It is why the deceleration of the vortical flow causes an expansion of the vortex. The passage shock is also disturbed by the strong interaction with the tip leakage flow. At low Reynolds number, the center of the tip leakage flow along the line "C" has values near -0.7 of the normalized helicity. This means that the roll-up is not sufficiently developed due to the small pressure difference until the tip leakage flow encounters the point with the maximum pressure difference. The passage shock is scarcely disturbed by the tip leakage flow. So, particle traces ejected around the center are still concentrated on its center after it passes the passage shock.

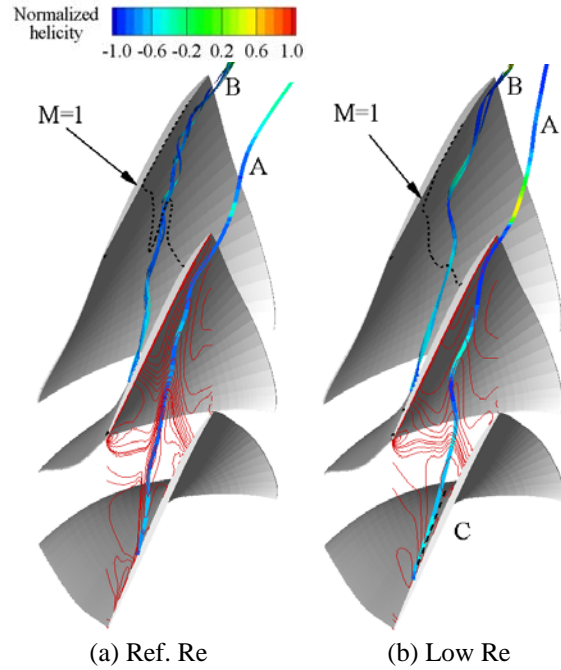


(a) Reference Re



(b) Low Re

Fig. 6 Non-dimensional static pressure distribution for the peak efficiency



(a) Ref. Re

(b) Low Re

Fig. 7 Static pressure contours, center of the tip leakage flow (A) and particle traces ejected around the center(B)

In order to inspect the structure of the separation on the blade surfaces, limiting streamlines in both cases are shown in Fig. 8. Similar streamlines except for the region near the tip are found on the pressure surface regardless of the Reynolds number. The limiting streamlines at the trailing edge near the tip are influenced by the tip leakage flow. The tip leakage flow encounters the pressure surface near the trailing edge as it proceeds to the downstream after being ejected near the pressure side leg of the passage shock. The limiting streamlines are more severely disturbed at the reference Reynolds number because the tip leakage flow has a strong roll-up and a large spiral motion in comparison to its counterpart. The limiting streamlines on the suction surface are significantly affected by the Reynolds number. At the reference Reynolds number, three separations could be found at the leading edge near the hub (A), at the trailing edge near the hub (B) and near the tip (C). The first is generated by the large incidence angle near the hub. The second is generally called as hub-corner-separation and frequently developed by the large deflection of the blade in the subsonic flow regime. The last is caused by the passage shock and located just behind the suction side leg of it. At the low Reynolds number, there are still three separations. However, the shape of the full-span separation (B') and the separation caused by the passage shock (C') is severely changed, while the separation at the leading edge (A') is slightly large in comparison to its counterpart (A). The separation line (C') is caused by the passage shock and located at slightly upstream of the separation focus (C) because the shock moves upstream as the Reynolds number is decreased. The hub-corner-separation at the reference Reynolds number grows large to be the full-span separation

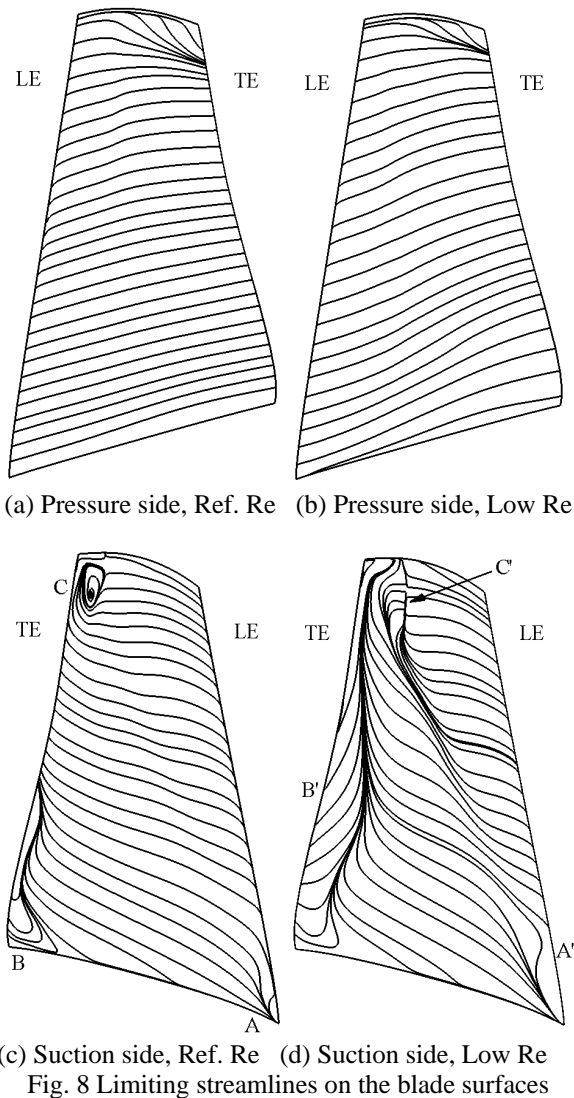


Fig. 8 Limiting streamlines on the blade surfaces

near the trailing edge. This phenomenon is also observed in the subsonic compressor rotor of the previous study (Choi et al.⁽⁷⁾). The interesting point is that two separations exist near the casing, where the former is caused by the passage shock in the supersonic regime and the latter by the back pressure in the subsonic regime.

Figure 9 shows entropy distributions at 50% chord and aero-station 2 to investigate where the loss is generated. Most of the loss is caused by the tip leakage flow, the casing boundary layer and the wake of the blade in both cases regardless of the Reynolds number. At the reference Reynolds number, the particle traces ejected before the suction side leg of the passage shock passes the high entropy region near the casing (A) at 50% chord. This means that the tip leakage flow generate large loss, interacting with the casing boundary layer. It is also found that the entropy is large on the pressure surface near the tip. This is caused by the growth of the boundary layer on the pressure surface behind the passage shock. At aero-station 2, the loss near the casing becomes large in comparison to the 50% chord because the casing boundary layer and the tip leakage flow have been mixed. The blade wake is thickened along the span

even though the separation occurs on the suction surface near the hub. This is why the passage shock makes the boundary layer on the blade surface to be thick above 70% span. By the way, there is a small vortex core (B) next to the blade wake near the casing and it generates relatively high entropy in comparison to the vicinity of it. This core is formed by the tip leakage flow ejected behind the suction side leg of the passage shock. At the low Reynolds number, the region with the high entropy expands. At 50% chord, the entropy is high near the casing because the boundary layer on the casing grows large by the large viscosity, but there is no core of the tip leakage flow because it is very weak. The entropy on the pressure surface is also high in the boundary layer. At the aero-station 2, the boundary layers on the endwall cause a large loss near the casing. The tip leakage flow near the trailing edge is so weak that the roll-up is not sufficiently formed. The wide region of the high entropy (C) is caused by the tip leakage flow ejected before the passage shock. The wake region increases in comparison to the reference Reynolds number due to the thick boundary on the blade surface and the separations on the suction surface at the trailing edge.

3.2 Loss Characteristics

To analyze the effects of the low Reynolds number on the loss characteristics, the total pressure loss was scrutinized in four loss categories available in a transonic axial compressor such as the profile loss, the tip leakage loss, the endwall loss and the shock loss using Denton's loss model.

The profile loss implies the loss generated by the blade itself except for the influences of the hub and the casing, and it is divided into two parts: the loss

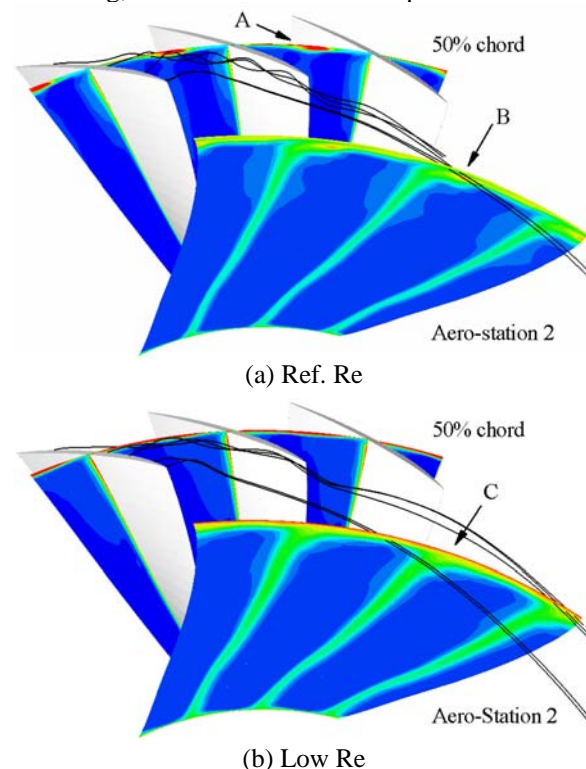


Fig. 9 Entropy distribution and particle traces ejected from the tip clearance at 50% chord and aero-station 2

generated in the boundary layers on the blade surface and the loss by the wake mixing. The loss generated on the suction surface is generally larger than that on the pressure surface because it is proportional to the cubic of the surface velocity. The surface velocity means the velocity at the outer edge of the boundary layer. The boundary layer loss coefficient was defined as the entropy increase per unit mass divided by the inlet relative dynamic head, and the equation is written as follows.

$$\zeta_{bl} = \frac{1}{0.5s \cos \beta_1} \int_0^c C_d \left(\frac{W_\delta}{W_1} \right)^3 dx \quad (2)$$

where the dissipation coefficient, C_d , is set to be equal to 0.002 as suggested by Denton and Cumpsty⁽²²⁾. The boundary layer loss calculated using Eq. (2) is shown in Fig. 10. Because the boundary layer loss is proportional to the cubic of the surface velocity on the blade as stated above, there is a close connection between the boundary layer loss and the inlet velocity profile.^(Choi et al.⁽¹⁸⁾) The overall distributions of the boundary layer loss in both cases are similar to each other since identical inlet velocity profile was imposed.

The trailing edge loss means additional loss generated at the trailing edge caused by the pressure mismatch between the trailing edge and the core flow region, the momentum decrement in boundary layer, and the blockage by the blade and displacement thickness. The trailing edge loss coefficient was non-dimensionalized by the exit relative dynamic head.

$$\zeta_{tr} = -\frac{C_{pb}t}{s \cos \beta_2} + \frac{2\theta}{s \cos \beta_2} + \left(\frac{\delta^* + t}{s \cos \beta_2} \right)^2 \quad (3)$$

$$C_{pb} = -\frac{p_b - p_2}{0.5\rho W_2^2}$$

When a separation develops at the trailing edge of the blade, the trailing edge loss coefficient is simplified as the following because the loss generated by the blockage is dominant.

$$\zeta_{tr} \cong \left(\frac{\delta^* + t}{s \cos \beta_2} \right)^2 \quad (4)$$

The trailing edge loss at the reference Reynolds number has a large value from the hub to 20% span because of the hub-corner-separation, but it diminishes steadily above 40% span since there is no separation. The trailing edge loss has a non-physical value above 90% span, because this region is included in the region where the tip leakage flow has major effects and assumptions used in the derivation of Eq. (3) are not valid. At the low Reynolds number, the large trailing edge loss is generated by the full-span separation at the trailing edge from the hub to 80% span, and it is larger than that at the reference Reynolds number along the full span.

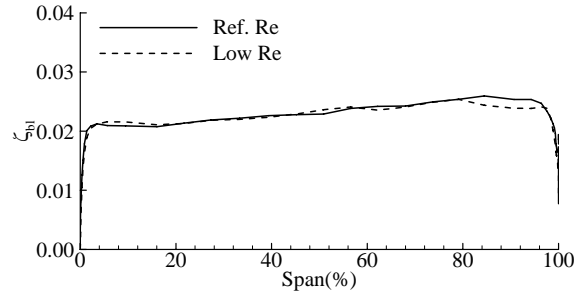


Fig. 10 Boundary layer loss along the span

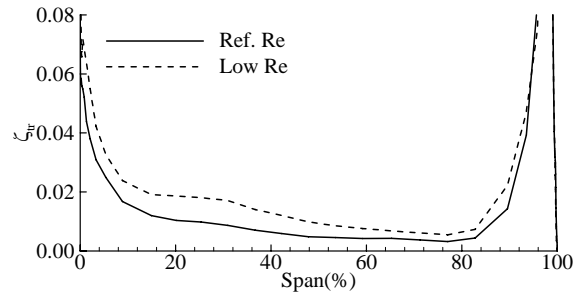


Fig. 11 Trailing edge loss along the span

Table 2 Integrated tip leakage loss and endwall loss

	ζ_{tl}	ζ_{el}
Ref. Re	0.004520	0.01364
Low Re	0.002064	0.01318

The tip leakage flow is mixed into the core flow and this mixing complicates the internal flow, resulting in a large loss. Assuming that the tip leakage flow is similar to a jet crossing the core flow, the loss coefficient can be derived. The loss due to the tip leakage flow is non-dimensionalized by the inlet relative dynamic head and written as follows.

$$\zeta_{tl} = \frac{2C_c}{s \cos \beta_1} \int_0^c \frac{\tau}{h} \left(\frac{W_\delta}{W_1} \right)^2 \left(1 - \frac{W_\phi}{W_\delta} \right) \sqrt{1 - \left(\frac{W_\phi}{W_\delta} \right)^2} dx \quad (5)$$

where the contraction coefficient, C_c , is set to be 0.8 and the variable τ/h is included in the integrand because the tip clearance and the blade height are not constant along the chord.

The loss generated in the boundary layer on the hub and the casing is called the endwall loss, which is divided into the secondary loss and the annulus loss. Generally, compared with an axial turbine, an axial compressor has a weak secondary flow and a thin boundary layer on the endwall because the blade is thin and the load at each stage is low. Although it is easy to think that the endwall loss in a compressor is much smaller than that in a turbine, the endwall loss is also important in a compressor because of the separations on the endwall induced by the adverse pressure gradient. The endwall loss coefficient was calculated using a method similar to the profile loss with the surface velocity relative to the endwall, and non-dimensionalized by the inlet dynamic head.

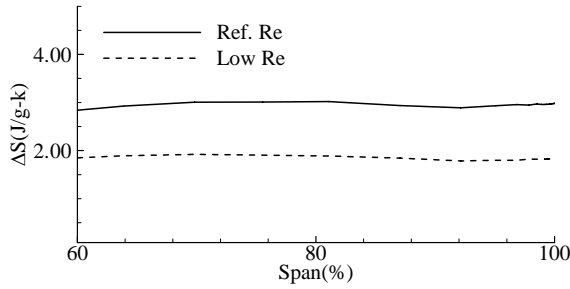


Fig. 12 Entropy generation caused by the passage shock along the span

$$\zeta_{el} = \begin{cases} \frac{T_1 \Delta S_{ew}}{0.5mV_1^2} & (\text{for stationary wall}) \\ \frac{T_1 \Delta S_{ew}}{0.5mW_1^2} & (\text{for moving wall}) \end{cases} \quad (6)$$

$$\Delta S_{ew} = \int_0^{A_s} \frac{C_d \rho V_\delta^3}{T} dA$$

The calculated tip leakage loss and endwall loss are shown in Table 2. The tip leakage loss in this study is reduced as the Reynolds number decreases. This tendency is same as that of the subsonic axial compressor in the previous study (Choi et al.⁽⁷⁾) and it is why the mixing between the tip leakage flow and the main flow becomes weak. By the way, only the endwall loss on the hub was calculated, because the loss on the casing is influenced by the tip leakage flow and also because it is not easy to classify the loss into a tip leakage loss and an endwall loss separately. The endwall loss on the hub is nearly same in both cases regardless of the Reynolds number.

Assuming that the passage shock is a single shock wave and it is sufficiently weak, the entropy generation is represented by a function of the static pressure as Eq. (7).

$$\Delta S \approx C_v \frac{\gamma^2 - 1}{12\gamma^2} \left(\frac{\Delta p}{p_1} \right)^3 + O \left(\frac{\Delta p}{p_1} \right)^4 \quad (7)$$

Because the passage shock exists above about 60% span from the hub, the entropy generation is shown from 60% span to the casing in Fig. 12. The entropy generation increases at the reference Reynolds number because the passage shock is strong so the static pressure rise is also large in comparison to the low Reynolds number.

This loss analysis revealed the following results about the relation of the each loss and the Reynolds number. First, some loss in a transonic axial compressor has a similar trend to a subsonic axial compressor. Namely, the boundary layer loss and the trailing edge loss are dependent on the inlet velocity profile and the separation at the trailing edge respectively. The tip leakage loss is reduced as the Reynolds number decreases. However, the endwall loss on the hub is nearly same regardless of the Reynolds number, and this is why the ratio of the

surface velocity on the hub to the inlet velocity is not changed by the Reynolds number and the boundary layer on the endwall is very thin. Second, the difference of the total pressure distribution along the span might caused by the passage shock and the full-span separation. Above 95% span, the total pressure ratio is nearly same as each other regardless of the Reynolds number. This means that the static pressure increment gained by the passage shock offsets the tip leakage loss, the shock loss and the endwall loss on the casing. The effect of the tip leakage flow is confined to this narrow region because of the small tip clearance. Below 60% span, the full-span separation at the low Reynolds number makes a large trailing edge loss and it could cause a large total pressure loss in this region. From 60% to 95% span, the advantages of the passage shock far surpass the trailing edge loss and the shock loss because the shock is a very efficient compression mechanism if the upstream Mach number is less than about 1.5. Therefore, the performance drop at the low Reynolds number is attributed to the weak passage shock and the full-span separation at the trailing edge.

4. Conclusion

The three-dimensional numerical simulation was conducted at two different Reynolds numbers, 1.17×10^5 and 1.17×10^6 , to study the effects of the low Reynolds number on the loss characteristics in a transonic axial compressor. The total pressure rise and the adiabatic efficiency decreased about 3 percent at the same normalized mass flow rate as the Reynolds number decreased. The relatively large viscosity added the dissipative effect on the flow and significantly affected the location and the intensity of the passage shock. The passage shock at the low Reynolds number moved upstream to the leading edge and its intensity decreased in comparison to that at the reference Reynolds number. This change caused by the low Reynolds number had large effects on the pressure distribution and the separation on the blade surface, the tip leakage flow. The pressure difference across the blade decreased as the Reynolds number was reduced, and it made the tip leakage flow to be weak and not to have a strong roll-up. The boundary layers on the blade surface grow by the large viscosity at the low Reynolds number and cause the full-span separation at the trailing edge. These changes of the internal flows also affected on the loss distribution. As the Reynolds number is reduced, the trailing edge loss is increased while the tip leakage loss and the shock loss are decreased. The boundary layer loss and the endwall loss are nearly constant regardless of the Reynolds number. At the reference Reynolds number, the efficient compression of the relatively strong passage shock offsets or surpasses the large loss caused by the tip leakage flow and the passage shock above 60% span. In addition, the full-span separation causes a large loss below 60% span at the low Reynolds number. As a result of these loss characteristics, the total pressure ratio and the

performance at the reference Reynolds number are larger than that at the low Reynolds number along the full span.

Acknowledgements

This work was supported by the Agency for Defense Development under the contract UD04006AD.

References

- 1) Weinberg, M., and Wyzykowski, J.: Powering unmanned air craft, *Aerospace Engineering*, 2001, pp. 23-26.
- 2) Castner, R., Shiappetta, S., Wyzykowski, J., and Adamczyk, J.: An engine research program focused on low pressure turbine aerodynamic performance, *ASME Paper*, 2002, GT-2002-30004.
- 3) Schreiber, H.-A., Steinert, W., and Küsters, B.: Effects of Reynolds number and free-stream turbulence on boundary layer transition in a Compressor Cascade, *Journal of Turbomachinery*, 2002, **124**, pp. 1-9.
- 4) Van Treuren, K. W., Simon, T., Von Koller, M., Byerley, A. R., Baughn, J. W., and Rivir, R.: Measurements in a cascade flow under ultra low Reynolds number conditions, *Journal of Turbomachinery*, 2002, **124**, pp. 100-106.
- 5) Matsunuma, T.: Effects of Reynolds number and freestream turbulence on turbine tip clearance flow, *Journal of Turbomachinery*, 2006, **128**, pp. 166-177.
- 6) Matsunuma, T., and Tsutsui, Y.: Effects of low Reynolds number on wake-generated unsteady flow of an axial-flow turbine rotor. *Int. J. of Rotating Machinery*, 2005, **2005**(1), pp. 1-15.
- 7) Choi, M., Baek, J. H., Chung, H. T., Oh, S. H., and Ko, H. Y.: Effects of the low Reynolds number on the loss characteristics in an axial compressor, *Proceedings of the Institution of Mechanical Engineers, Part A (Journal of Power and Energy)* (accept)
- 8) Adamczyk, J., Cestina, L., and Greitzer, E. M.: The role of tip clearance in high-speed fan stall, *Journal of Turbomachinery*, 1993, **115**, pp.28-39.
- 9) Copenhaver, W. W., Mayhew, E. R., Hah, C., and Wadia, A. R.: The effect of tip clearance on a swept transonic compressor rotor, *Journal of Turbomachinery*, 1996, **118**, pp. 230-239.
- 10) Masake, O., and Kaji, S.: Numerical analysis of transonic compressor rotor flow near stall points, *ASME paper*, 1997, 97-GT-68.
- 11) Chima, R. V.: Calculation of tip clearance effects in a transonic compressor rotor, *Journal of Turbomachinery*, 1998, **120**, pp. 131-140.
- 12) Gerolymos, G. A., and Vallet, I.: Tip-clearance and secondary flows in a transonic rotor, *Journal of Turbomachinery*, 1999, **121**, pp. 751-762.
- 13) Hoeger, M., Fritsch, G., and Bauerm, D.: Numerical simulation of the shock-tip leakage vortex interaction in HPC front stage, *Journal of Turbomachinery*, 1999, **121**, pp. 456-468.
- 14) Park, J. Y., Chung, H. T., and Baek, J. H.: Effects of shock-wave on flow structure in tip region of transonic compressor rotor, *Int. J. of Turbo & Jet Engines*, 2003, **20**, pp. 41-62.
- 15) Denton, J. D.: Loss mechanisms in turbomachines, *Journal of Turbomachinery*, 1993, **115**, pp. 621-656.
- 16) Strazisar, A. J., Wood, J. R., Hathaway, M. D., and Suder, K. L.: Laser anemometer measurements in a transonic axial-flow fan rotor, NASA Technical Paper-2897, 1989.
- 17) Choi, H. S., and Baek, J. H.: Computations of nonlinear wave interaction in shock wave focusing process using finite volume TVD schemes, *Computers and Fluids*, 1995, **25**, pp. 509-525.
- 18) Choi, M., Park, J. Y., and Baek, J. H.: Effects of the inlet boundary layer thickness on the loss characteristics in an axial compressor, *Int. J. of Turbo & Jet Engines*, 2006, **23**, pp. 51-72.
- 19) Park, J. Y., Choi, M., and Baek, J. H.: Effects of axial gap on unsteady secondary flow in one-stage axial turbine, *Int. J. of Turbo & Jet Engines*, 2003, **20**, pp. 315-333.
- 20) Baldwin, B. S., and Lomax, H.: Thin layer approximation and algebraic model for separated turbulent flows, AIAA Paper 78-257, 1978.
- 21) U. S. Standard Atmosphere, in http://modelweb.gsfc.nasa.gov/atmos/us_standard.html
- 22) Denton, J. D., and Cumpsty, N. A.: Loss mechanisms in turbomachines, *ImechE Paper*, 1987, No. C260/87.

Appendix

Nomenclature

A_w	: Endwall area
C	: Chord length
C_c	: Contraction coefficient
C_d	: Dissipation coefficient
C_{pb}	: Base pressure coefficient
C_v	: Specific heat capacity
h	: Blade height
m	: Mass flow rate
p	: Static pressure
p_b	: Static pressure at the trailing edge
r	: Radius
s	: Pitch
S	: Entropy generation
S_{ew}	: Entropy generated on the endwall
t	: Blade thickness
T	: Static temperature
V	: Absolute velocity on the inertial coordinate
V_δ	: Surface velocity relative to the endwall
v_θ	: Whirl velocity

v_r : Radial velocity
 W : Relative velocity
 W_δ : Surface velocity on the blade surface
 $W_{\delta p}$: Surface velocity on the pressure surface
 $W_{\delta s}$: Surface velocity on the suction surface

Greek

β : Flow angle
 γ : Specific heat ratio
 Δ : Increment or Decrement
 δ^* : Displacement thickness
 θ : Momentum thickness
 ρ : Air density
 ζ_{bl} : Boundary layer loss coefficient
 ζ_{el} : Endwall loss coefficient
 ζ_{tl} : Tip leakage loss coefficient
 ζ_{tr} : Trailing edge loss coefficient
 τ : Height of the tip clearance

Subscripts

1 : Inlet in the computational domain
2 : Outlet in the computational domain